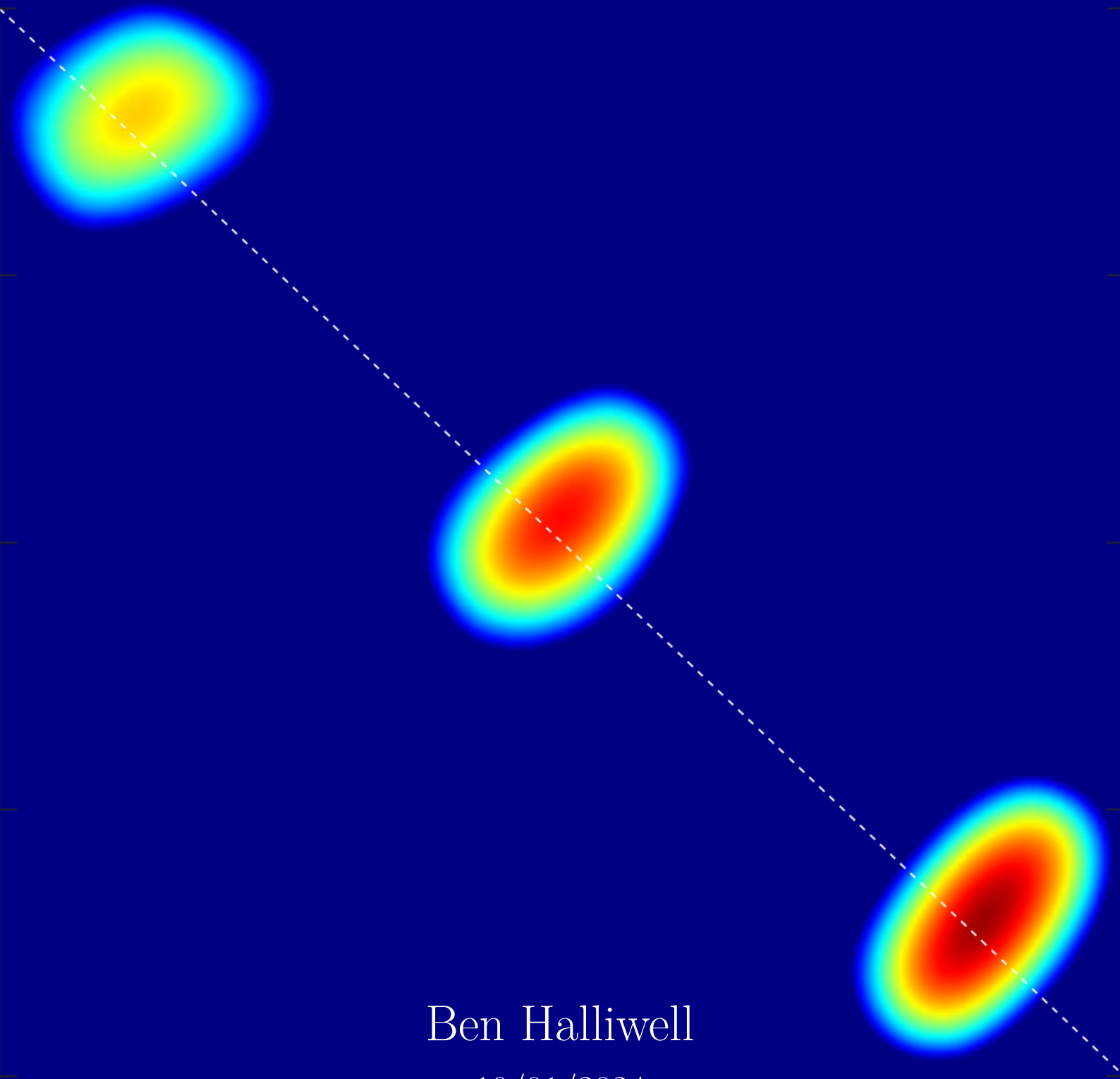# Weld Inspection & Failure Analysis

MENGM0058: Structural Integrity & Non-Destructive Evaluation

Ben Halliwell

10/01/2024

Department of Mechanical Engineering

Image: 3 embedded cracks located on a weld face.

A. Non-Destructive Evaluation

A.1 Introduction

Ultrasonic non-destructive evaluation (NDE) is critical to many modern inspection processes, as it can quickly and safely reveal sub-surface defects, especially in safety critical industries, such as nuclear energy. In 1985, a pipe in the Surry 2 nuclear reactor catastrophically failed, fatally injuring four workers [4]. The primary factor in this incident was localised thinning of the pipe wall from 13 to 0.38mm, due to erosion-corrosion, which was not picked up by the primitive ultrasonic detection unit. This is one of countless examples of incidents that could have been prevented with improved ultrasonic detection. However, overly conservative or time-consuming NDE increases the repair and inspection time, ultimately increasing the cost of maintenance of the nuclear reactor. Therefore, any ultrasonic NDE process must be quick and accurate to maximise effectiveness.

A.2 Initial Process Design

Firstly, the ultrasonic transducer parameters should be chosen. All the parameters are coupled, so expressions relating each parameter to each other must be determined. The first element position (FEP) is defined as the distance between the edge of the weld toe and the centre of the first element and determines the angle of incidence between the ultrasonic wave and the crack. Since the crack is approximately one-dimensional, the ray should hit the crack orthogonally to maximise the amplitude of the reflected rays. Since the transducer cannot be placed directly above the crack due to the uneven weld surface, the reflection of the ray off the inner wall of cooling pipe will give a stronger signal than the direct ray (Fig. 1a). This also means the optimum FEP varies based on the crack depth, with a greater FEP preferable for shallower cracks. As stated in the brief, the transducers will not be scanned transverse to the weld to minimise operation time, so a constant FEP value must be chosen (Fig. 1b).
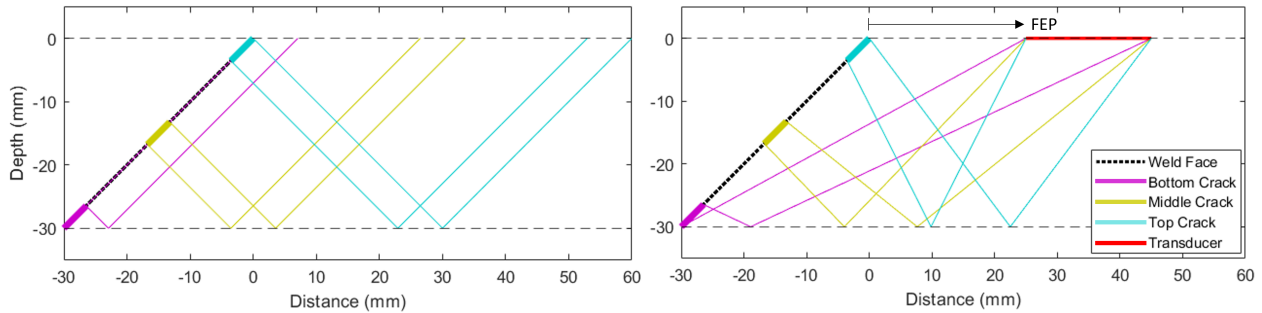

Figure 1: (a) orthogonal incidence of ultrasonic rays for 5mm cracks, (b) incidence from single FEM

The optimum FEP was defined as the position which gives the optimum mean angle of incidence: $\min(|\bar{\theta} - 90|°)$. Figure 2 shows the optimum FEP is negatively proportional to the length of the transducer transverse to the weld. However, the FEP cannot be less than half the element width (w) as no part of the transducer can be situated on the weld: $\text{FEP}_{\text{opt}} = \max(25 - 0.35L_t, w/2)$ [mm].
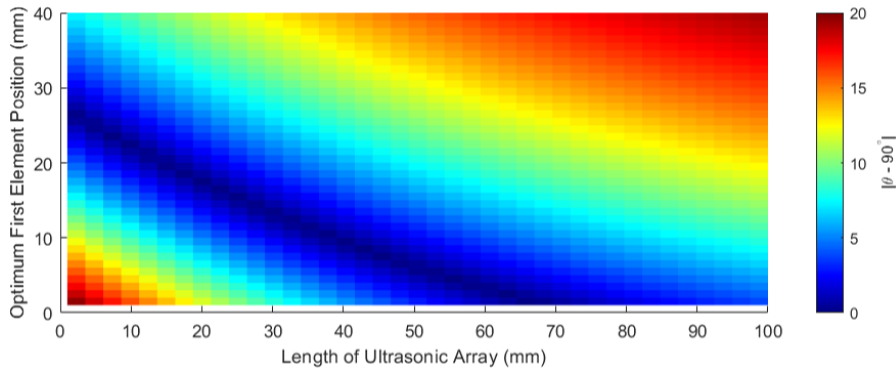

Figure 2: Optimum FEP based on array length (dark blue)

Huygens' wave model was used to estimate the lateral focusing resolution of the ultrasonic array (Fig. 3) and validate the predicted effects of changing transducer parameters. The length of the transducer transverse to the weld L_t depends on the number of elements (n), element width and pitch (p): $L_t = (n - 1)p + w$. Increasing the element pitch above half a wavelength ($\lambda/2$) leads to under-sampling of the signal based on Nyquist-Shannon sampling theory [1].
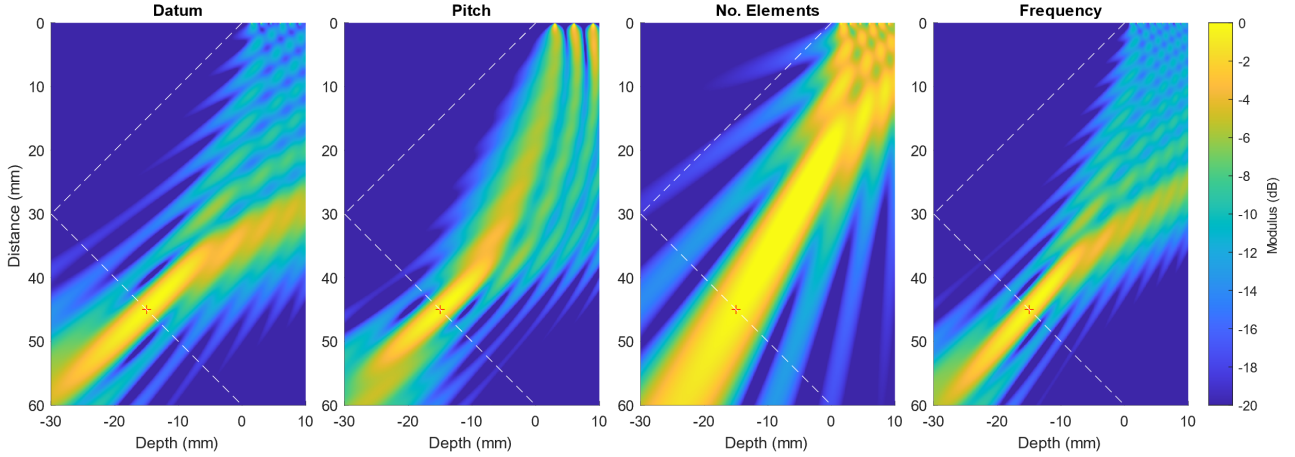
Figure 3: (a) n = 64, f = 2MHz, p = $\lambda/2$, w = p - 0.05. (b) Same as (a) but p = λ, (c) n = 16, (d) f = 3MHz

However, a greater pitch improves the angular resolution and manufacturability of the array, albeit with an increase in artefacts such as grating lobes due to undersampling (Fig. 3b). The limited angle Nyquist criteria: $p = (1 + \sin(\theta_s))^{-1}\lambda$ [1] was used to determine the element pitch for a steering angle (θ_s) of 45°, equal to the weld angle, giving $p = 0.59\lambda$. The element width is often designed to be as close to the pitch as possible [1]. From the Huygens' model, the width was found to have a negligible impact on the lateral focusing resolution, and since smaller width elements are harder to manufacture, larger width elements are preferred. The minimum distance between elements stated in the brief is 0.05mm, therefore the element width is $w = p - 0.05\,[\text{mm}]$. Decreasing the number of elements has a detrimental impact on the resolution of the image (Figure 3c). Since the Micropulse FMC controller can already accomodate up to 64 elements, it is assumed the cost benefit of fewer elements is negligible, and so the number of elements was chosen to be **64**. Finally, increasing the centre frequency of the signal (f_c) has a significant positive impact on the focusing resolution (Fig. 3d); however, increasing f_c reduces the amplitude at that frequency, decreasing the signal-to-noise ratio (SNR). The signal-to-noise ratio was calculated as the ratio of the root mean square (RMS) of the frequency spectrum within the spectral range specified in the brief (0.44 to 1.56 f_c) compared to outside it (Fig. 4). The centre frequency was chosen to satisfy the common industry rule of thumb SNR > 3 [2], giving f_c = **2.7MHz**. The other parameters can then be calculated: $\lambda = c/f_c = 2.2$mm, giving p = **1.32mm**, w = **1.27mm** and FEP = **0.64mm**. Huygens' model predicts that the lateral resolution varies from 4.9mm at the bottom of the weld [-30,30] to 2.8mm at the top [0,60]. It should be noted the rays reflected off the back wall can be detected by scanning the area below the backwall, generating a flipped image (Fig. 3).
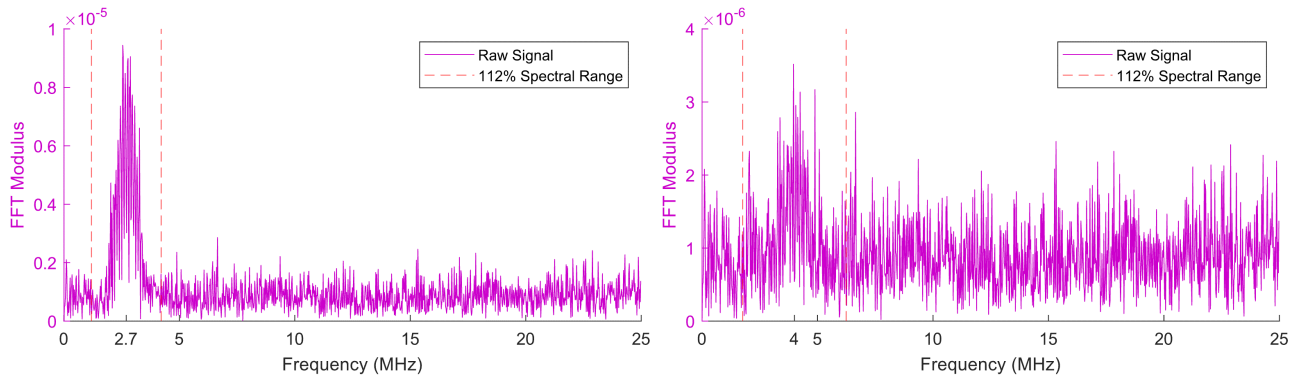

Figure 4: FFT of signal (a) f = 2.7MHz, SNR = 3 (b) f = 4MHz, SNR = 1.3

The '_POINTS_NO_NOISE' scenario was used to find the exact frequency spectrum emitted by the transducer, allowing accurate fitting of a Hann and Gaussian window (Fig. 5a). In both the frequency and time-domain response, the Hann window is marginally better; as it follows the frequency spectrum more accurately for f < 1.7, f > 3.6 MHz (Fig. 5a), resulting in a greater absolute amplitude, determined from the Hilbert transform, of the backwall signal (Fig. 5b).
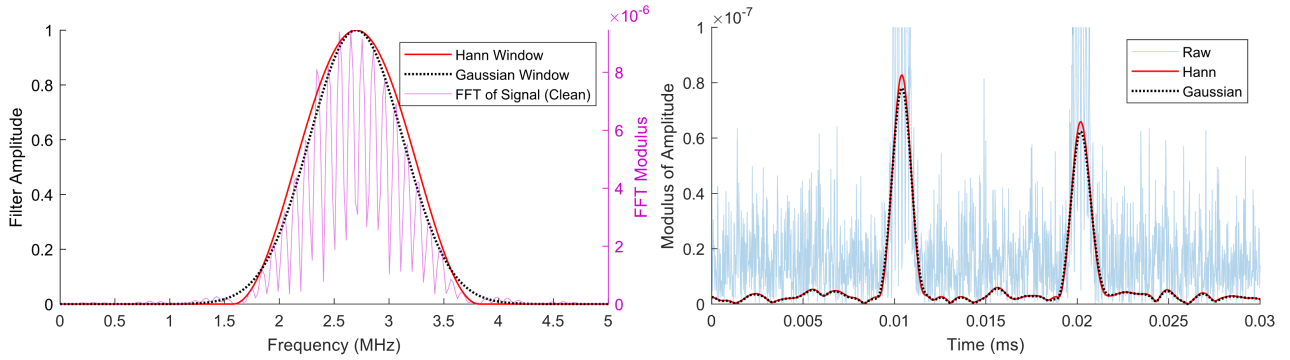
2

Figure 5: (a) Fitting the filter to noiseless frequency spectrum, (b) Effect of filter on time-domain

A.3 Advanced Process Design

The defects can be imaged using the Total Focusing Method (TFM), which relates the time-of-flight (τ_{kl}) of the signal to reach any arbitrary point $[x_i, y_j]$ in the component, from the transmitting (T_k) and receiving R_l array element, to the A-scan data (G_{kl}) (Fig. 5b) for each transmitter-receiver pair.

$$I_{\text{TFM}}(x_i, y_j) = \left| \sum_{kl} G(t = \tau_{ijkl})_{kl} \right|, \text{ where } \tau_{ijkl} = \frac{1}{c} \left(\sqrt{(x_i - T_k)^2 + y_j^2} + \sqrt{(x_i - R_l)^2 + y_j^2} \right) \quad (1)$$

Alternatively, the Phase Coherent Imaging (PCI) algorithm can be used. TFM predominantly considers the modulus of time domain signal, whilst only indirectly considering the phase (ϕ), whereas PCI utilises a phase-dependent statistical weighting function, such as the circular coherence factor (F_c), to suppress grain noise [3] (Eq. 2).

$$I_{\text{PCI}}(x_i, y_j) = F_c(x_i, y_j) I_{\text{TFM}}(x_i, y_j) \text{ where } F_c(x_i, y_j) = 1 - \sqrt{\text{var}(\cos(\phi_{ij})) + \text{var}(\sin(\phi_{ij}))} \quad (2)$$

The image can be easily generated using a quadruple nested loop (i, j, k, l); however, this is extremely slow, with a mean computation time of 0.4 seconds per pixel (Fig. 6) for TFM. At this speed, producing a single sufficiently resolved image, 300x300 pixels, would take 10 hours, which is not practical for any imaging application. The limiting factor in this code is interpolation for $t = \tau_{tr}$, so instead of linear interpolation between values, a more computationally efficient nearest-neighbour interpolation was used in version 2. This halved the computation time, but created artefacts in the signal due to information loss. The most significant improvement was in version 3, which used vectorisation when interpolating between x and y, reducing the number of nested loops to two (k, l).
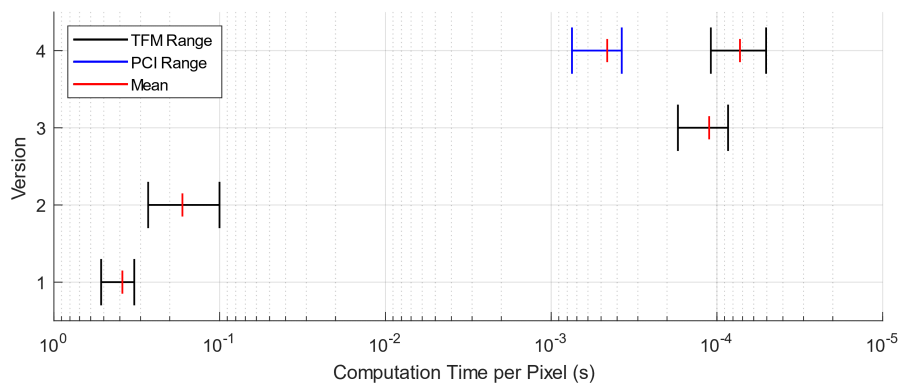

Figure 6: Optimising Computation Time of Code for TFM and PCI (mode = POINTS)

Minor improvements were implemented in version 4, such as pre-computing τ_{ijkl} and improved memory allocation, which reduced the mean computation time to $70\mu s$ per pixel, or 6 seconds to produce a 300x300 pixel image. The variability in computation time is due to different image sizes. Smaller images have fewer pixels so the initialisation time is large compared to the nested loop time, increasing the computation time per pixel. Also, memory issues are encountered when generating the largest images, with both algorithms failing at images > 600x600 pixels. Calculating the variance in the F_c function was computationally intensive, making PCI five times slower than TFM, and therefore only incorporated into the fourth version of the algorithm (Fig. 6)

3

A.4 Known Test

PCI reduces the noise by 20dB more than TFM (Fig. 7), so the bottom crack can be more easily distinguished from noise. PCI also reduces the amplitude of the backwall at [0,60], allowing top cracks to be distinguished from the backwall automatically by the sizing algorithm (Fig. 8a-b). However, PCI causes slight distortion in the image, which is noticeable at the backwall.
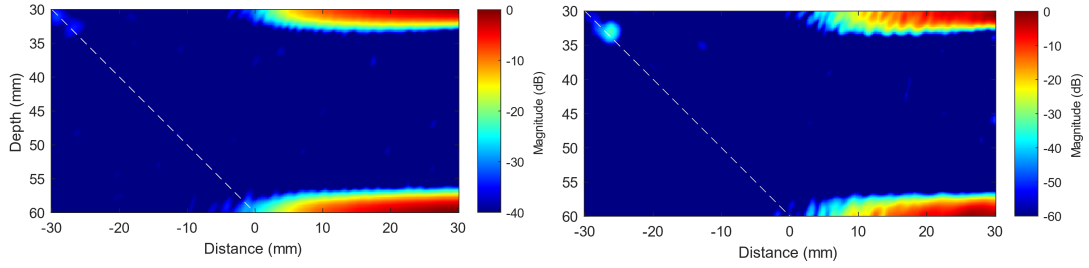

Figure 7: Image of Bottom Crack generated by (a) TFM and (b) PCI Imaging Algorithms

To size the cracks, the image was thresholded at -15dB (-25dB for PCI), relative to the maximum amplitude within the weld region [-30 to 0, 30 to 60], to reject noise whilst still observing the bottom crack (Fig. 8a-b, 9a). The MATLAB function *bwlabel* was used to identify the shape and centre of the resulting image clusters (red dots). It was assumed small clusters are noise, so a minimum threshold of 0.2% of the image size was implemented (green cross). Additionally, cracks are only expected on the fusion faces, so a maximum threshold of 2mm from the fusion face was also implemented (black square). Any clusters meeting these criteria were re-thresholded (Fig. 9b) at the crack threshold: -6dB (-12dB for PCI) relative to the maximum amplitude within the cluster. This ensures consistency at different depths, as the bottom cracks are much lower in amplitude than the top cracks. Using *pdist2*, the maximum distance between any two points within the crack (magenta) was calculated.
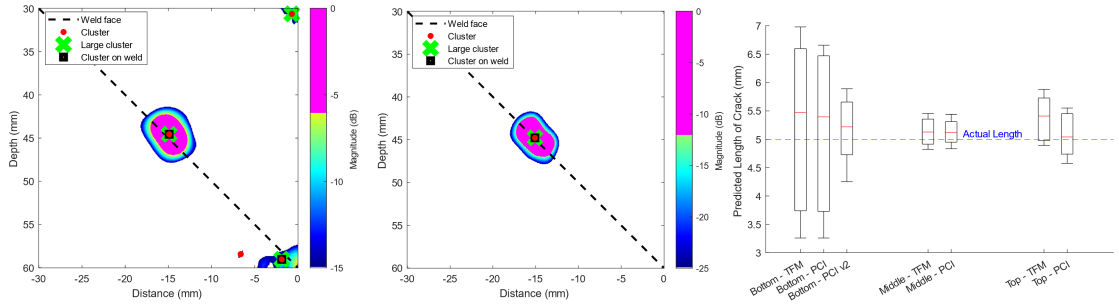

Figure 8: Sizing of the middle crack: (a) with TFM, (b) with PCI, (c) Sizing Performance [50 trials per crack depth per imaging algorithm]

PCI performs slightly better than TFM at sizing the cracks since TFM produces a large number of false positives, such as characterising the backwall reflection [0,60] as an additional crack (Fig. 8a). Both algorithms perform poorly at sizing the bottom crack (Fig. 8c). Bottom cracks are often over-sized as the crack threshold is too low for the bottom crack allowing background noise to distort the shape (Fig. 9a-b). Under-sizing can also occur, as the leading and trailing edge of the crack produce a much higher amplitude signal than in the middle, causing the algorithm to identify two smaller cracks rather than a single one (Fig. 9c). Therefore, in the second PCI sizing algorithm, the crack threshold for bottom cracks is -6dB. Then *pdist2* is used to find the maximum distance between any point in the crack and the base of the crack [30,-30] (Fig. 9c), as it is assumed this is where a bottom crack would initiate from, significantly improving the sizing performance (Fig. 8c). The maximum diameter of the Point Spread Function (PSF) ellipse using PCI is around 4mm at all depths and as predicted by Huygens', top crack flaws are more eccentric as the lateral resolution is improved.

A.5 Blind Trial

The simulation was performed parallel to the weld (Z) at 2mm intervals, much smaller than the 15mm length of the transducer parallel to the weld stated in the brief. Therefore, 150 scans are required giving a computation time of 75 minutes, assuming the PCI algorithm takes 30 seconds. This is reasonable, assuming the data collected from the actual ultrasonic array can be pre-processed off-site. If real-time images need to be generated, then the resolution must be decreased or the TFM algorithm could be used. For the simulation mode **'ug20032'**, five cracks were identified on the weld face (X_{45}): two in the middle and at the bottom of the weld and one at the top (Tab. 1, Fig. 10).
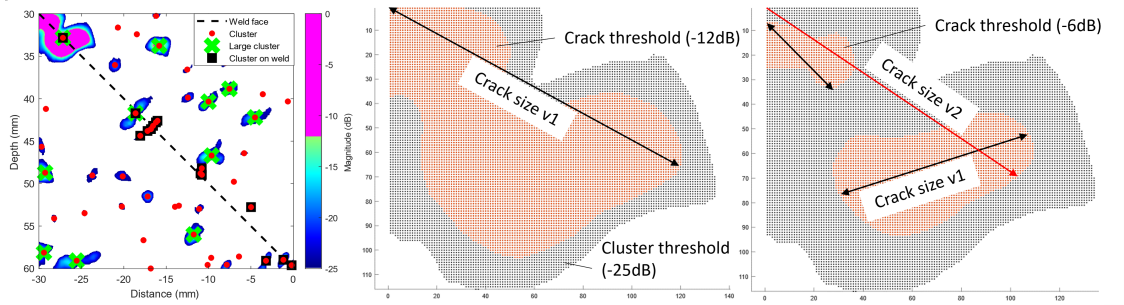
Figure 9: Sizing of the bottom crack: (a) with PCI (b) oversized crack (c) undersized crack

The smallest bottom crack has a crack depth $a = 3.4$mm, which is smaller than the PSF. Therefore, it is impossible to accurately determine the bottom crack depth for a frequency of 2.7MHz. Since PCI is better at suppressing noise than TFM, higher central frequency (f_c) arrays could be used without noise becoming too intense. For the bottom crack, f_c was increased to 3.4MHz giving $a = 3.0$-3.1mm and 4.4mm for the bottom and top cracks respectively, greater than the PSF of 2.6mm. Since the middle cracks are at the most favourable incidence angle (Fig. 1b), f_c was increased to 4.2MHz. At this frequency, two co-linear cracks $\approx$5mm each are predicted instead of a single 12mm crack, although this could be due to the shape distortion produced by PCI. At these high frequencies (HF), there are a large number of false positives, so low frequency (LF) imaging is required to filter out false positives prior to HF imaging. Therefore, 2.7MHz is more robust and is preferred, as it is assumed the array is limited to one constant central frequency. The 95% confidence bound for the crack depths was determined as ± 2 standard deviations of the data recorded in (Fig. 8c), adjusted for the over-estimated mean.

Table 1: Crack Sizing Blind Trial: mode='ug20032'

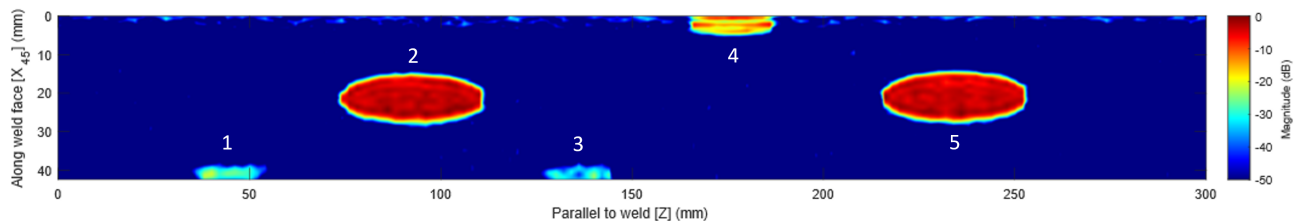| Crack Number	1	2	3	4	5
Z-position at centre of crack (mm)	44	92	136	176	234
Length of crack in X_{45}-direction [LF] (mm)	3.4	11.5	4.2	4.5	12.1
Length of crack in X_{45}-direction [HF] (mm)	3.0	5.5,4.1	3.1	4.4	4.7,5.8
Crack depth [a] (mm) 95% confidence	2.5-3.9	5.5-5.8	3.3-4.7	3.9-5.0	5.9-6.2
Crack length [2c] (mm)	18$\pm$2	38$\pm$2	20$\pm$2	22$\pm$2	38$\pm$2

Figure 10: Planar Image of the Defects along the Weld Face [X_{45}], generated with the PCI algorithm at 2.7MHz

A.6 Conclusion

Overall, PCI can be used to predict size of cracks along the weld face with reasonable confidence for a central frequency of 2.7MHz. Higher central frequencies can be used to more accurately size small cracks, but require an initial LF check, to reject false positives. To further improve the ultrasonic inspection process, the sizing algorithm should be tested on known cracks of different shapes and sizes, instead of just 5mm cracks so the effect of varied crack size can be measured. Also, testing should be performed on multiple cracks per scan position, to assess the performance at sizing collinear cracks. Finally, different weighting functions for the PCI algorithm could be tested to improve noise rejection, allowing the frequency of ultrasound, and therefore resolution of the image, to be further increased.

References

[1] P. D. Wilcox and J. Zhang, "Quantification of the effect of array element pitch on imaging performance," *IEEE Transactions on Ultrasonics, Ferroelectrics, and Frequency Control*, vol. 65, no. 4, pp. 600–616, 2018.

[2] Iowa State University - Center for Nondestructive Evaluation. Signal-to-noise ratio. Accessed on 28/12/2023. [Online]. Available: https://www.nde-ed.org/Physics/Waves/signaltonoise.xhtml

[3] J. Zhang, B. W. Drinkwater, and P. D. Wilcox, "Comparison of ultrasonic array imaging algorithms for nondestructive evaluation," *IEEE Transactions on ultrasonics, ferroelectrics, and frequency control*, vol. 60, pp. 1732–1745, 2013.

B. Part B

B.1 Introduction

This report details the structural integrity assessment for a feedwater transfer pipe (FTP) situated in a Boiling Water nuclear Reactor (BWR). The function of an FTP is to supply hot water to the reactor pressure vessel (RPV) to produce steam and regulate the RPV temperature during normal operation. Additionally, it must supply cooling water to the RPV in an emergency scenario to prevent thermal runaway of the reactor core. One of the multiple emergency cool-down systems is the high-pressure coolant injection system (HPCI). The design-basis event (DBE) considers a valve failure in one of the four feedwater pipes requiring the HPCI to inject cold water downstream of the valve, to maintain the flow of cooling water. This causes a temperature gradient between the cooled inner wall of the pipe and the hot outer wall, which retains the heat from the hot water, potentially causing failure of the FTP. The following analysis will follow the recommended fracture assessment procedure {[5], 7.1.1}[1] in the industry standard for the structural integrity of pipes, BS7910:2019 [5]. This standard has been rigorously tested and validated against experimental data, ensuring a compelling argument can be provided to the regulatory body if needed.

B.2 Stresses

Primary stresses are stresses which could cause plastic collapse [5], such as those induced by internal pressure and thermal shock. The pipe is approximated to be a thick-walled cylinder in plane strain, constrained at both ends. This gives the hoop ($\sigma_{\theta\theta}$), radial (σ_{rr}) and axial (σ_{zz}) stress at a radial distance (r) [6]:

$$\sigma_{\theta\theta}(r) = A\left(1 + \frac{r_o^2}{r^2}\right), \ \sigma_{rr}(r) = A\left(1 - \frac{r_o^2}{r^2}\right), \ \sigma_{zz}(r) = 2\nu A \quad \text{where} \ A = \frac{r_i^2 P}{r_o^2 - r_i^2} \tag{3}$$

where $r_i = 400$mm and $r_o = 430$mm are the inner and outer radii of the pipe, $P = 7$ MPa [7] is the internal pressure and $\nu = 0.305$ is the Poisson's ratio [10]. It can be seen that the hoop stress is the greatest (Figure 11a) at a maximum of 97MPa. The thermal analysis [8] (Figure 11b) is strongly conservative, as it assumes the maximum possible initial temperature of the water in the FTP, minimum injection temperature of the cooling water, and minimum pipe-to-water heat transfer. This is a difference of 232°C, compared to a minimum possible temperature difference of 118°C [7]. No fluid dynamic effects were simulated in the model. Cool water injected by the HPCI is denser than the pre-existing hot water, which can cause a stratified flow with cold water along bottom of the pipe [4] leading to global bending of the pipe due to thermal contraction. However this only causes mild fatigue damage [4], so not modelling the fluid dynamics is a valid simplification (Figure 11b).
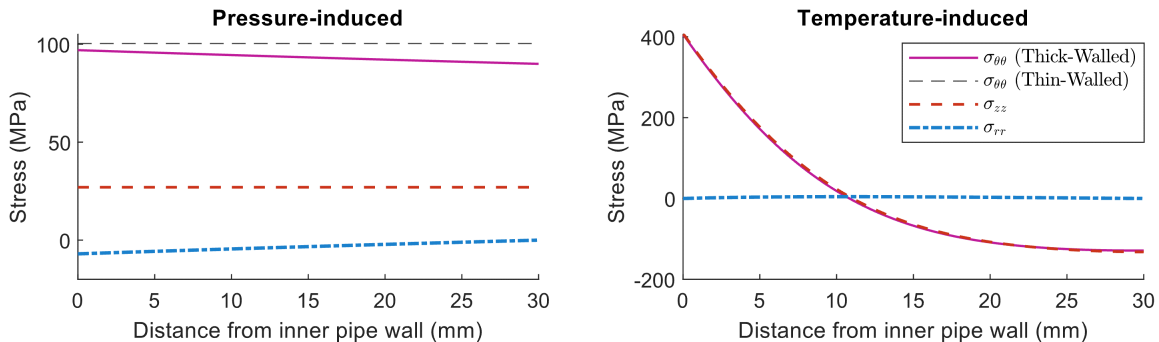

Figure 11: Primary Stresses due to: (a) Internal pressure for a thick-walled cylinder in plane, (b) Temperature variation through-thickness after 10 seconds cooling

The primary stress components were summed and linearised across the flaw (Figure 12a), allowing the local membrane (σ_m) and bending (σ_b) stress to be calculated {[5], 6.4.2}:

$$\sigma_m = \frac{\sigma_1 + \sigma_2}{2}, \ \sigma_b = \frac{\sigma_1 - \sigma_2}{2} \tag{4}$$

The hoop stress is larger than the axial stress, giving $\sigma_{m,p} = 366$ MPa and $\sigma_{b,p} = 135$ MPa. Therefore, the cracks aligned longitudinally with the pipe will experience higher stresses, making the repair patch especially vulnerable to failure. Secondary stresses are stresses which cannot cause plastic collapse [5], such as residual stresses induced by welding. The residual stresses calculated by Technova Analytics

---

[1]Curly braces denote the section in BS7910:2019 from which the relevant information is retrieved from

[9] give $\sigma_{m,s} = 178$ MPa and $\sigma_{b,s} = $ -28 MPa (Figure 12b). These measurements were taken around the circumferential welds but should be applicable to the axial welds, as the welding process is identical.
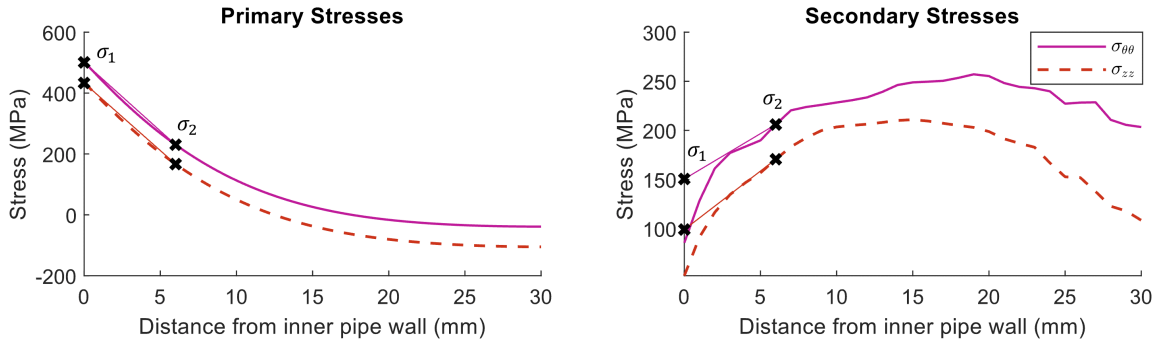

Figure 12: Linearisation of (a) Primary Stress, (b) Secondary Stress

B.3 Failure Assessment Diagram

For the parent material, stress-strain data can be used to formulate the Failure Assessment Line (FAL or $K_{r,\max}(L_r)$) using the Option 2 method {[5], 7.3.4}:

$$K_{r,\max}(L_r) = \left(\frac{E\varepsilon_{ref}}{L_r\sigma_Y} + \frac{L_r^3\sigma_Y}{2E\varepsilon_{ref}} \right)^{-0.5} \quad \text{for } \{0 \leq L_r < L_{r,\max}\}, \quad \text{else } K_{r,\max}(L_r) = 0 \tag{5}$$

where the elastic modulus $E = 181$ GPa, the yield strength $\sigma_Y = 431$ MPa [10] and ε_{ref} is the true strain corresponding to the true stress $\sigma_{ref} = L_r\sigma_Y$. The maximum load ratio is defined as the point above which plastic collapse occurs $L_{r,\max} = (\sigma_Y + \sigma_U)/(2\sigma_Y)$, based on the yield and ultimate tensile strength $\sigma_U = 644$ MPa. The material properties used in equation 5 are mean values [10], as specified by {[5],7.1.3.2}. Using the ambient or elevated temperature had a negligible impact on the FAL as it is normalised by σ_Y. For the weld material, only simple data is available [10], so the less accurate Option 1 method must be used {[5],7.3.3}. C-Mn steels, such as the weld material [10], can exhibit discontinuous yielding {[5],7.1.3.6}, so the discontinuous FAL Option 1 is used:

$$K_{r,\max}(L_r) = \left(1 + \frac{1}{2}L_r^2 \right)^{-0.5} \text{ for } \{0 \leq L_r < 1\}, \quad K_{r,\max}(L_r) = \left(\lambda + \frac{1}{2\lambda} \right)^{-0.5} \text{ for } \{L_r = 1\} \tag{6a}$$

$$K_{r,\max}(L_r) = K_{r,\max}(L_r = 1)L_r^{(N-1)/(2N)} \quad \text{for } \{1 < L_r < L_{r,\max}\}, \quad K_{r,\max}(L_r) = 0 \quad \text{for } \{L_r \geq L_{r,\max}\} \tag{6b}$$

with coefficients $\lambda = 1 + (E\varepsilon_{\max})/\sigma_U$ and $N = 0.3(1 - \sigma_Y/\sigma_U)$. For the weld material, $E = 178.9$GPa, $\varepsilon_{\max} = 0.15$, $\sigma_Y = 402$, and $\sigma_U = 569$ MPa. The FAL curves can be seen in figure 14.

B.3.1 Load Ratio

Equation 7 was used to calculate the load ratio ($L_r = \sigma_{ref}/\sigma_Y$) for an internal surface flaw in a long[2], thin-walled pipe {[5],P.8.2}:

$$\sigma_{ref} = M\sigma_{m,p} + \frac{2\sigma_{b,p}}{3(1 - \alpha'')^2}, \quad M = \frac{1 - a/(BM_t)}{1 - a/B}, \quad M_t = \sqrt{1 + 1.6\left(\frac{c^2}{r_iB}\right)}, \quad \alpha'' = \frac{a/B}{1 + B/c} \tag{7}$$

where the flaw height $a = 6$mm, the maximum flaw half-length $c = 12$mm and the section thickness $B = 30$mm, giving $\sigma_{ref} = 468$ MPa. This gives a load ratio of **1.09** and **1.16** for the parent and weld material respectively, using the mean yield strength at 300° C. At this temperature, the strength properties of both the parent and weld material are reduced by around 15% compared to ambient. This is conservative as the crack region is predicted to have a temperature of 75-150°C after 10 seconds of cooling [8]. This also ensures any material degradation, such as erosion-corrosion, or flow-induced fatigue [4] can occur without reducing the material properties below expected.

B.3.2 Fracture Ratio

K_{Ic} testing was only performed for the parent material at -90° C [10]. This temperature is unrepresentative of the actual conditions the pipe experiences, as the minimum temperature of the cooling water is 8°C [10], making the test sample more brittle than in reality. Instead, the fracture toughness K_{mat} was determined from ASTM E 813 (Fig. 13) [11] giving J_{mat} of 153 and 189 N/mm, and K_{mat} values of 175 and 193 MPa$\sqrt{\text{m}}$ for the parent and weld material respectively (Eq. 8).

---

[2]'Long' is defined as $W \geq 2(c + B)$. W = 5m, c = 12mm, B = 30mm

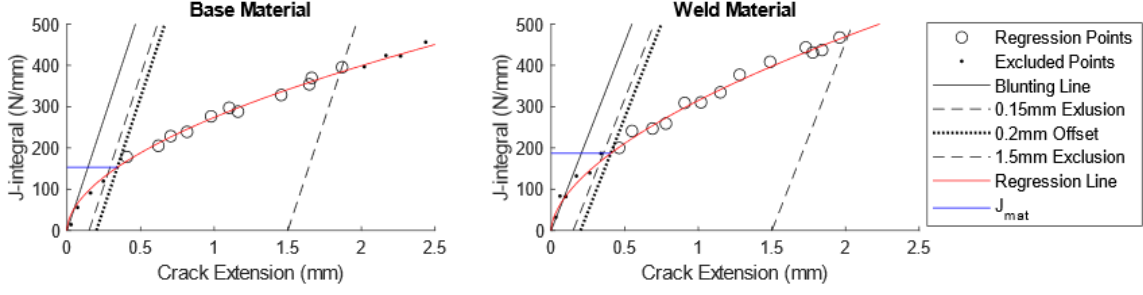$$K_{mat} = \sqrt{\frac{EJ_{mat}}{1-\nu^2}} \tag{8}$$

Figure 13: Determining J_{mat} using ASTM E 813 for the (a) base material and (b) weld material

The stress intensity factor: $K_I = Y\sigma\sqrt{\pi a}$ depends on the applied stress, stress concentration (k) and magnification (M) factors {[5],M.1}.

$$(Y\sigma)_p = Mf_w(k_{tm}M_{km}M_m\sigma_{m,p} + k_{tb}M_{kb}M_b[\sigma_{b,p} + (k_m-1)\sigma_{m,p}]), \quad (Y\sigma)_s = M_m\sigma_{m,s} + M_b\sigma_{b,s} \tag{9}$$

The crack is conservatively re-characterised as orthogonal to the pipe wall as advised [12], rather than along the weld. Cracks which are not angled orthogonally to the the applied stress experience some mode III shear loading, instead of pure mode I uniaxial loading, which decreases the effective stress intensity: $K_{eff} = K_I\sin(\beta)^2$ [13]. For a weld angle $\beta = 45°$, re-characterisation could be twice as conservative than in reality. Also, since the defect is small compared to the cross-sectional area of the pipe, the net area factor is negligible: $f_w = 1.00$ {[5],M.2}. Additionally, misalignment of the two pieces joined by the weld can cause a stress concentration[3] {[5],D.1}:

$$k_m = 1 + \frac{\sigma_{s,axial}}{\sigma_m} + \frac{\sigma_{s,angle}}{\sigma_m} \quad \text{where} \quad \frac{\sigma_{s,axial}}{\sigma_m} = \frac{6e}{B_1(1-\nu^2)}\left(\frac{1}{1+(B_2/B_1)^{0.6}}\right) \tag{10}$$

where the thickness of the two sections are B_1 and B_2 and the eccentricity is e. Ideally, there should be no eccentricity or thickness variation for the repair pipe as it reuses the piece originally cut out. However, the wrong repair patch could be welded on and some misalignment is expected as welding occurs on-site. In the scenario where the thickest and thinnest repair patch are accidentally swapped, but the pipe is well-aligned, $e = 1.4$mm, $B_1 = 28.8$mm and $B_2 = 30.2$mm [14], giving a $\sigma_{s,axial}/\sigma_m = 0.16$. It is also assumed there is no angular misalignment of the weld $\sigma_{s,angle}/\sigma_m = 0$, giving $k_m = 1.16$. Since the FTP is straight and no notches or holes are expected to be present [12], the membrane and bending stress concentration factors k_{tm}, k_{tb} are assumed to be 1 {[5],6.4.4}. The interface between the parent and weld material induces a local region of stress concentration ($M_{k,m}, M_{k,b}$). BS7910 does not explicitly give a suitable equation for this factor at the root of a weld toe {[5],M.11.1.4}, referring to [15]. The crack geometry lies outside of the bounds of the relevant equation, but for low normalised weld bead root widths ($\frac{w}{B}$) and high relative crack depths ($\frac{a}{B}$), M_k approaches 1. Therefore M_k was assumed to be 1. The stress intensity magnification factor for an internal defect on a thick-walled cylinder {[5],M.7.2.2} is only applicable for $t/r_i > 0.1$, whereas for the pipe, $t/r_i = 0.075$. Instead, the pipe was approximated as a plate, which is valid since the bulging factor was negligible $M = 1.00$ (Eq. 7, {[5],M.6.1}). The stress intensity magnification factor[4] for membrane stress {[5],M.4.1.2.2} is:

$$M_m = \left[M_1 + M_2\left(\frac{a}{B}\right)^2 + M_3\left(\frac{a}{B}\right)^4\right]\frac{gf}{\phi} \tag{11a}$$

$$M_1 = 1.13 - 0.09\left(\frac{a}{c}\right), \quad M_2 = \frac{0.89}{0.2+(a/c)} - 0.54, \quad M_3 = 0.5 - \frac{1}{0.65+(a/c)} + 14\left(1-\frac{a}{c}\right)^{24} \tag{11b}$$

$$g = 1 + \left[0.1 + 0.35\left(\frac{a}{b}\right)^2\right](1-\sin(\theta)^2), \quad f = \left[\left(\frac{a}{c}\right)^2\cos(\theta)^2 + \sin(\theta)^2\right]^{0.25}, \quad \phi = \sqrt{1+1.464\left(\frac{a}{c}\right)^{1.65}} \tag{11c}$$

and for bending[4] {[5],M.4.1.3.2} it is:

$$M_b = [H_1 + (H_2-H_1)\sin(\theta)^q]M_m, \quad \text{where} \quad q = 0.2 + \frac{a}{c} + 0.6\frac{a}{B} \tag{12a}$$

---

[3]Eq. 10 refers to an axially-misaligned longitudinal weld (i.e. along the repair patch)

[4]Valid for $0 < a/(2c) \le 0.5$. a = 6mm, c = 12mm.

$$H_1 = 1 - 0.34\frac{a}{B} - 0.11\frac{a^2}{cB},\; H_2 = 1 + \left[-1.22 - 0.12\frac{a}{c}\right]\frac{a}{B} + \left[0.55 - 1.05\left(\frac{a}{c}\right)^{0.75} + 0.47\left(\frac{a}{c}\right)^{1.5}\right]\left(\frac{a}{B}\right)^2 \quad (12b)$$

where θ is the angle around the semi-elliptical crack. For the deepest point in the crack ($\theta = 90°$) $M_m = 0.92$, $M_b = 0.69$ and for the shallowest point $M_m = 0.72$ and $M_b = 0.67$. Therefore, the deepest point in the crack is the limiting factor, giving $K_{I,p} = 64.4$ MPa$\sqrt{\text{m}}$ and $K_{I,s} = 19.9$ MPa$\sqrt{\text{m}}$. The fracture ratio can then be determined {[5],7.3.6,R.2.2}:

$$K_r = \frac{K_{I,p} + VK_{I,s}}{K_{mat}} \quad \text{where } V = 0.4 \text{ for } \{L_r > 1.05\} \tag{13}$$

giving $K_r = $ **0.41** and **0.37** for the parent and weld material respectively (Figure 14).

B.4   Sensitivity Analysis

To account for variation in uncertainties in the model, a sensitivity analysis was performed (Figure 14). The thickness of the pipe (B) was varied between 28.8-30.2mm, and the inner diameter (d_i) varied between 798.8-801.2mm [14]. The aspect ratio $a/2c$ was varied between 0.25 [12] and the upper bound of equations 11 & 12, 1.0, with the crack depth a varied between 0-6mm. Additionally, the time at which the thermal stresses occur was varied between 10, 15 and 20 seconds [8], as it is unclear which of these scenarios is the worst. The residual tolerance was also varied by ±41 MPa to account for statistical variation [9]. For the parent material, the yield strength (σ_Y) was varied between 428-433 MPa and the ultimate tensile strength (σ_U) was varied between 642-647 MPa. Due to insufficient data, the strength of the weld material was not varied. The locus was drawn from $a= 0$ to 24mm for c = 12mm, the point which equations 11 & 12 become invalid. For small crack depths, any increase in a decreases average membrane stress over the crack, which causes the decrease in L_r (Fig. 12a). At larger crack sizes, a/B becomes important causing an increase in in L_r (Eq. 7). Also for large cracks, the highest stress intensity factor occurs at the surface, rather than the deepest point of the crack.
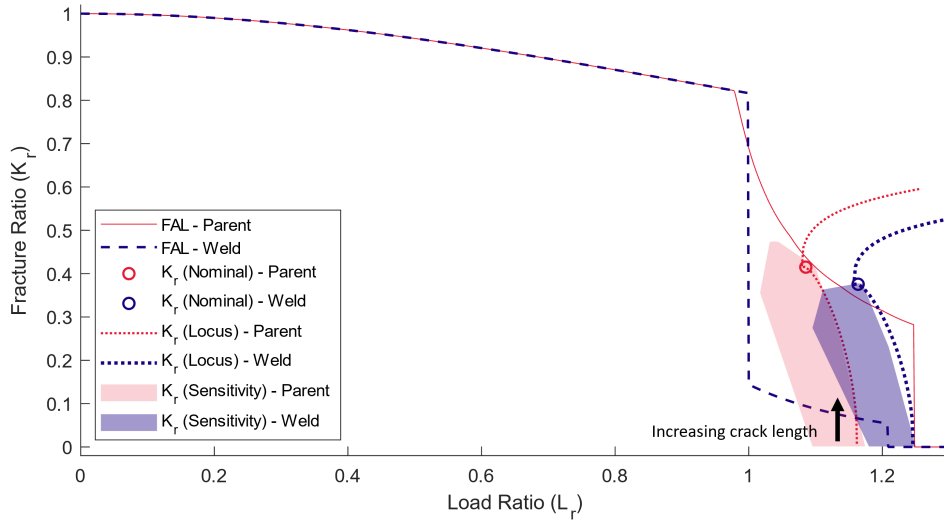

Figure 14: Failure Assessment Diagram for the parent and weld material[5].

B.5   Discussion

Both the parent and weld material have differing material properties, causing heterogeneous plastic deformation. For a weld interface flaw in a thin-walled cylinder, the load limit ratio is equal to the mismatch in yield strength $F_E^M/F_E^P = M = \sigma_Y^W/\sigma_Y^P = 0.94$ {[5],P.13.5.3}, as the weld material is under-matched. Since $F_E^M/F_E^P = M$, this cancels out the combined parent-weld discontinuous FAL {[5],I.3.7.3} and combined yield strength {[5],I.3.2} effectively meaning the parent material has no beneficial contributing effect and the weld material is the limiting case.

This means that despite the parent material assessment point remaining below the FAL, the pipe is expected to fail under the current DBE. However, it is only predicted with medium certainty that the pipe would fail, as the weld FAL is based on the less accurate Option 1. If detailed stress-strain data

---

[5]All equations used in figure 14 are the long form equations, and are therefore applicable outside the bounds of equations used for 6mm crack analysis. Some equations shown in the report have been shortened to conserve space, see relevant section(s) in BS7910 [5] for full equation.

could be obtained for the weld, the Option 2M FAL {[5],I.3.8} could be determined, which may give a significantly different result. Additionally, the material properties, temperature-induced stress and flaw re-characterisation were all conservatively determined and incorporating the uncertainties only reduces the predicted confidence of failure by moving the assessment point closer to the FAL.

The consequences of failure of pipes in nuclear reactors can be severe. In 1985, a pipe in the Surry 2 nuclear reactor catastrophically failed, causing the discharged water to flash to steam, fatally injuring four workers [4]. However, this could not happen in the analysed scenario. The HPCI delivers cool water, preventing the flashing occurring, and the FTP downstream of the valve is in the workerless radiation-controlled area of the power plant [12] rather than the turbine room in Surry 2. Even if failure of the pipe were to occur, it would be ductile failure, due to the high L_r value. This is beneficial, as there may be visible deformation or potentially a leak-before-break (LBB) condition {[5],F.1} allowing the HPCI to be shut-down before catastrophic failure occurs. Finally, in this scenario, there would still be three operational feedwater lines, each of which can cool the reactor on its own [12] plus redundant cooling mechanisms: low-pressure coolant injection, automatic depressurisation and core spray [16]. Therefore, four simultaneous feedwater valve failures, plus four simultaneous, catastrophic feedwater pipe failures and failure of the other remaining coolant systems would have to occur for the DBE to cause a nuclear meltdown, which is unreasonably unlikely.

To improve the accuracy of the analysis, additional material experiments should be performed for the weld material. This will save costs if a complete redesign can be avoided. An improved tensile test is strongly recommended to record the stress-strain data during an experiment, as this would allow the option 2M FAL method to be used. Additionally, tensile testing at at a reduced temperature is recommended, to measure the strength at a more representative temperature than $300°C$ or ambient. If however, the analysis still shows that the weld metal is expected to fail, an overmatched weld metal ($\sigma_Y^W > \sigma_Y^P$) should be selected. If the pipe is still not sufficient, a complete redesign is required, although this should be a last resort given the large associated cost [12].

B.6 Conclusion
Based on the current analysis, it can be shown with medium confidence that the weld metal will fail for the DBE. Therefore, it is recommended that further analysis is conducted into the material properties of the weld to obtain a more accurate parent-weld FAL before submitting a safety case to the regulatory board. Nonetheless, if failure were to occur the consequences would be low, given the risk to human life is low, and multiple redundant systems are available to prevent nuclear meltdown.

References

[4] US Nuclear Regulatory Commission, "CR-4731 Residual Life Assessment of Major Light Water Reactor Components - Overview," 1989, sec. 6, pp. 73-104. [Online]. Available: https://www.nrc.gov/docs/ML0403/ML040360166.pdf

[5] British Standards Institution, "BS 7910:2019: Guide to methods for assessing the acceptability of flaws in metallic structures," 2019.

[6] C. E. Truman, "Mechanics of Materials Handout 2021-22," 2021, page 57.

[7] H. Fenwick, "LBB Energy BWR design data," Unpublished document, LBB Energy, February 5 2019, doc. no. 93388203R1, note: this fictional document was provided in the coursework.

[8] P. Jankowski, "Thermal shock of a BWR Main Feedwater Line – simplified analysis," Unpublished document, Parrett Associates, November 14 2019, note: this fictional document was provided in the coursework.

[9] Technova Analytics, "00492M: Ferritic steel pipe girth welds, residual stress," Unpublished document, job ref. 04492M, note: this fictional document was provided in the coursework.

[10] LBB Energy, "Materials test data relevant to BWR Main Feedwater Line pipework," Unpublished document, doc. no. 87669540, note: this fictional document was provided in the coursework.

[11] M. Janssen, J. Zuidema, and R. Wanhill, *Fracture mechanics: fundamentals and applications*. CRC Press, 2004, pages 167-171. [Online]. Available: https://doi.org/10.1201/9781482265583

[12] LBB Energy, "LBB Energy BWR feedwater pipe design considerations," doc. no. 90473811, note: this fictional document was provided in the coursework.

[13] L. Pook, "The effect of crack angle on fracture toughness," *Engineering Fracture Mechanics*, vol. 3, no. 3, pp. 205–218, 1971. [Online]. Available: https://doi.org/10.1016/0013-7944(71)90032-4

[14] Hever Johnson, *MFL WPS 131-FW-4 Welding Procedure Specification*, MFL Corporation, April 09 2020, note: this fictional document was provided in the coursework.

[15] Y.-H. Zhang, T. London, and D. DeBono, "Developing Mk Solutions for Fatigue Crack Growth Assessment of Flaws at Weld Root Toes in Girth Welds," in *International Conference on Offshore Mechanics and Arctic Engineering*. American Society of Mechanical Engineers, 2018. [Online]. Available: https://doi.org/10.1115/OMAE2018-77067

[16] USNRC Technical Training Center, "Boiling Water Reactor (BWR) Systems." [Online]. Available: https://www.nrc.gov/reading-rm/basic-ref/students/for-educators/03.pdf